

Bistatic Passive Tracking via CSI Power

Zhongqin Wang, *Member, IEEE*, J. Andrew Zhang, *Senior Member, IEEE*,
Kai Wu, *Member, IEEE*, Kuangda Chen, Min Xu, *Member, IEEE*, Y. Jay Guo, *Fellow, IEEE*

Abstract—Accurate object tracking in Integrated Sensing and Communication (ISAC) applications remains challenging due to limited signal bandwidth, sparse antenna arrays, and clock asynchronism inherent in bistatic transceiver deployments. This paper proposes *PowerSense*, a real-time passive tracking framework that operates directly on the power of Channel State Information (CSI). Although CSI phase carries fine-grained information, its time-varying distortions require complex processing, which introduces additional interference during tracking. Instead, this work solely relies on CSI power for accurate sensing. We first remove all CSI phase offsets through a self-conjugate operation, yielding phase-independent CSI power. A cascaded Fast Fourier Transform (FFT) is then applied to extract delay, angle-of-arrival (AoA), and Doppler features, followed by object detection, outlier removal, and continuous trajectory estimation via an Extended Kalman Filter (EKF). To enable fine-grained motion sensing, the estimated target positions are further used to extract refined micro-Doppler signatures. Using 3.1 GHz LTE and 5 GHz WiFi bistatic signals with a 20 MHz bandwidth, our indoor experiments achieve a median tracking error of 0.4 m, without performing any pre-deployment system calibration, while simultaneously extracting clear and unambiguous micro-Doppler signatures of the tracked target.

Index Terms—Passive Tracking, CSI Power, Bistatic Sensing, Micro-Doppler, WiFi, LTE, ISAC, PMN.

I. INTRODUCTION

PERCEPTIVE Mobile Networks (PMN) [1] are redefining wireless communication by integrating environmental sensing into existing mobile infrastructures, forming a new paradigm known as Integrated Sensing and Communication (ISAC) [2], [3], where radio signals simultaneously enable data transmission and environmental perception. By extracting physical-layer features such as Channel State Information (CSI), ISAC systems can sense surrounding objects, human activities, and environmental dynamics [4], [5] without relying on dedicated sensing waveforms. Among various sensing tasks, passive object tracking has gained particular attention due to its broad applications in indoor localization, occupancy monitoring, device-free safety systems, and drone surveillance, while requiring no active participation from the target. In addition to sensing benefits, passive tracking enhances communication performance by enabling mobility-aware resource allocation, channel prediction, and interference mitigation, underscoring its dual utility within PMNs.

Despite its advantages, communication-signal-based sensing faces several practical issues. First, many widely deployed

communication systems operate with narrow bandwidths (e.g., 1.4-20 MHz in LTE), which fundamentally limits delay resolution. Second, the small number of antennas in typical Multiple-Input Multiple-Output (MIMO) deployments constrains the achievable spatial resolution. More critically, in bistatic sensing setups where transceivers operate without a unified clock, timing offsets (TO) and carrier frequency offsets (CFO) introduce time-varying random phase distortions across subcarriers and time samples in CSI measurements. A variety of phase compensation techniques have been proposed [6], including CACC [7], Differential CACC (DCACC) [8], [9], CASR [10], and reference-path methods [11], [12]. While these approaches are effective in mitigating TO and CFO, they often introduce interference artifacts or nonlinear transformations that degrade the estimation accuracy of key sensing parameters, including delay, Angle of Arrival (AoA), and Doppler Frequency Shift (DFS). These limitations highlight the need for more robust solutions for bistatic passive sensing.

To achieve accurate bistatic passive tracking in practical deployments, two critical challenges need to be addressed.

1) *Hardware-induced phase offsets affecting AoA estimation.* Hardware-induced phase variations across Rx antennas, such as those caused by differences in cables, connectors, and front-end components, can lead to phase mismatches. In addition, each hardware initialization (i.e., powering on the device) introduces a random initial phase offset on each channel due to imperfections in the Phase-Locked Loop (PLL) [13]. The initial phase introduced by the PLL is fixed once the system is locked, but varies randomly across different hardware initializations due to the unpredictable locking process. These hardware-related phase offsets pose a major challenge to accurate AoA estimation. To compensate for this, per-session antenna calibration is typically required, which increases system complexity and reduces deployment scalability.

2) *Clock asynchronism compensation-induced Doppler ambiguity affecting localization and sensing.* In bi-static systems, both TO and CFO distort CSI phase over frequency and time. Existing phase compensation techniques typically rely on a reference signal to eliminate them through conjugate multiplication. However, these reference signals, while assumed to capture only static components, often include target-induced motion signals. As a result, such compensation introduces mirrored Doppler artifacts, where Doppler shifts at $+f^D$ and $-f^D$ exhibit similar amplitudes. Despite being symmetric in the Doppler domain, these mirrored components correspond to different delay and AoA values, making it difficult to determine which sign of f^D represents the true target motion. This ambiguity injects noise into trajectory estimation and obscures fine-grained micro-Doppler signatures, thereby reducing the reliability of passive motion sensing.

Zhongqin Wang, J. Andrew Zhang (Corresponding Author), Kai Wu, Kuangda Chen, Min Xu are with the School of Electrical and Data Engineering and the Global Big Data Technologies Centre, University of Technology Sydney, Sydney 2007, Australia. E-mail: {zhongqin.wang, andrew.zhang, kai.wu, kuangda.chen, min.xu}@uts.edu.au

Y. Jay Guo is with the Global Big Data Technologies Centre, University of Technology Sydney, Sydney 2007, Australia. E-mail: jay.guo@uts.edu.au

In this work, we propose *PowerSense*, a calibration-free and real-time bistatic passive tracking framework based on CSI power. In addition to accurate trajectory estimation, *PowerSense* produces unambiguous Doppler signatures that accurately reflect human motion dynamics based on the estimated positions. It operates on commercial communication platforms with bistatic configurations. A human subject moves within an indoor environment while CSI is continuously collected for passive sensing. The target remains entirely device-free, allowing tracking based solely on signal reflections and scattering without requiring any equipment to be carried.

We first compute the CSI power by multiplying each CSI sample with its complex conjugate, thereby removing phase offsets caused by hardware imperfections and clock asynchronism in a simple and effective manner. We then design a signal-processing pipeline that extracts motion-related features from the CSI power, including delay, AoA, and DFS. The compensated real-valued CSI power is then transformed from the frequency domain to the delay domain using a single-sideband delay Inverse Fast Fourier Transform (IFFT). Static clutter removal is then applied to suppress background reflections and isolate motion-induced components. Subsequently, a two-dimensional FFT across the antenna and temporal dimensions jointly estimates the AoA and Doppler features. Building on these extracted features, an improved Constant False Alarm Rate (CFAR) detector is employed to identify valid targets, followed by a weighted joint optimization module for outlier suppression. Finally, an Extended Kalman Filter (EKF) fuses the delay, AoA, and Doppler measurements to achieve continuous and real-time trajectory tracking.

To further enhance motion analysis, we leverage the estimated target position to extract clearer and unambiguous micro-Doppler features. For each short-time window, we select the 3D FFT coefficient corresponding to the peak delay-AoA-Doppler bin. This 3D selection functions as a spatiotemporal filter, effectively suppressing interference from irrelevant locations and motions. Owing to its low computational cost, the window can slide with a small step size (e.g., 2 samples at 1 kHz), enabling high temporal resolution. The selected coefficients are then concatenated over time and processed by a refined Doppler FFT, producing temporally resolved and unambiguous micro-Doppler signatures.

Our main contributions are summarized as follows:

- 1) We introduce *PowerSense*, the first bistatic passive tracking framework that operates directly on CSI power. By discarding phase, the method removes random distortions caused by hardware imperfections and clock asynchronism, thereby avoiding complex phase compensation and calibration. Building on this property, we design a lightweight FFT-based processing pipeline for real-time object tracking with reduced computational overhead and enhanced tracking robustness.
- 2) We propose a position-guided micro-Doppler extraction that incorporates spatial filtering into motion analysis. By leveraging target-specific delay-AoA estimates, the method can suppress Doppler ambiguity introduced by clock-asynchronism compensation and produces unambiguous Doppler signatures for fine-grained motion interpretation.
- 3) We develop a prototype using a NI Massive MIMO

testbed as the base station (BS) and a USRP device as the user equipment (UE), equipped with a custom tool for uplink CSI extraction. Operating in a 1Tx-3Rx bi-static configuration without clock synchronization or prior antenna calibration, the proposed *PowerSense* achieves a median tracking error of 0.4 m, with a computation delay under 2 ms per update on a standard laptop (MacBook Pro 2019, 2.6 GHz 6-core Intel i7 processor), outperforming DCACC-based methods [8], [9] in accuracy and deployment practicality. The system additionally provides accurate micro-Doppler signatures that open up opportunities for enhanced sensing applications.

II. RELATED WORK

This section presents an overview of passive tracking techniques using communication signals, which can generally be categorized into two main approaches: signal model-based and deep learning-based methods. Signal model-based techniques rely on traditional signal processing algorithms to interpret CSI, whereas deep learning-based approaches leverage pre-collected data to train predictive models. Currently, deep learning methods [14]–[16] have attracted growing interest due to their potential to improve generalization across different environments. However, deep learning-based methods face two major challenges: limited labeled data and variability in signal characteristics across different conditions. Unlike implicit features in text and image fields, CSI provides physical features such as delay, AoA, and Doppler, which correspond to target positions while also mitigating the impact of static environmental differences during feature extraction [17]. More importantly, ensuring real-time performance remains a key consideration. Given these factors, the following discussion will focus on signal model-based methods, which offer a more practical and efficient solution for passive tracking.

Some works have explored passive object sensing using bistatic Long-Term Evolution (LTE) signals. In [18], coarse-grained parameters such as the Reference Signal Received Power (RSRP) and Reference Signal Received Quality (RSRQ) are used to detect airborne drones. In [19], [20], CSI is extracted from LTE signals and the CASR method is employed to mitigate clock asynchronism, enabling applications including respiration-rate estimation, vehicle speed estimation, vehicle counting, and soil-moisture sensing.

Complementing these LTE-based efforts, many studies have focused on WiFi-based bistatic systems for indoor passive tracking. Doppler-based methods [21] often use CASR to remove the random phase offsets and typically rely on multiple spatially distributed transmitter-receiver pairs. However, such methods introduce non-linear noise in delay estimation. In addition, since different body parts produce different Doppler reflections, the receivers may observe inconsistent motion components, which hinders long-term tracking performance. Widar2.0 [7] and mD-Track [22] adopt a CACC-based processing pipeline and formulate joint estimation as a maximum likelihood estimation (MLE) problem. However, their performance heavily depends on accurate initial guesses for MLE, which are generally unavailable in practical deployments. SHARP [12] employs a compressed-sensing based approach to

remove TO and constructs a reference path to compensate CFO for activity classification. However, performing compressed sensing each time incurs substantial computational overhead, making it unsuitable for real-time applications. JUMP [11] searches for a stable reference path to first eliminate TO and then jointly estimates delay and AoA from the compensated CSI. However, JUMP does not utilize Doppler information in tracking. This omission is significant, as Doppler provides high resolution and strong noise suppression capability that can greatly enhance the accuracy of delay and AoA estimation. WiDFS [8] and WiDFS 2.0 [9] propose differential CACC techniques that apply simple yet effective linear transformations to the raw CACC output, which can remove random phase distortions and strongly suppress Doppler mirroring. Building on this foundation, WiDFS introduces a lightweight framework that first extracts the dominant DFS of a moving subject and subsequently estimates AoA and delay for tracking. WiDFS 2.0 further extends this approach by extracting multiple Doppler components from different body parts to improve overall tracking accuracy. However, both systems rely on antenna calibration to achieve accurate AoA estimation.

In comparison, this work differs from these methods in several key aspects. First, instead of correcting random phase distortions, we directly operate on CSI power, fully discarding phase and eliminating the need for any phase-related calibration. Second, we employ a 3D FFT-based joint estimation of Doppler, delay, and AoA, which requires no calibration for AoA estimation and does not rely on prior knowledge of the target's initial position. Third, the low computational latency of our pipeline enables more frequent position updates, supporting accurate and robust real-time object tracking.

III. SIGNAL MODELS AND SYSTEM OVERVIEW

This section formulates the bistatic CSI model and provides an overview of the proposed PowerSense system.

A. Bi-static CSI Model

Each CSI measurement is denoted as $CSI_{i,j,k}$, where i , j , and k represent the receiver antenna index, subcarrier index, and CSI packet index, respectively. The CSI in the presence of a moving target is expressed as:

$$CSI_{i,j,k} = H_{j,k}^e H_i^h (H_{i,j}^S + H_{i,j,k}^X), \quad (1)$$

where

$$\begin{cases} H_{j,k}^e = e^{-J(\varphi_{j,k}^{\text{TO}} + \varphi_k^{\text{CFO}})}, \\ H_i^h = e^{-J\varphi_i^h}, \\ H_{i,j}^S = \rho_{i,j}^S e^{-J2\pi f_j \tau_i^S} + \mathbb{H}_{i,j}^S, \\ H_{i,j,k}^X = \rho_{i,j,k}^X e^{-J2\pi f_j \tau_{i,k}^X} + \mathbb{H}_{i,j,k}^X. \end{cases} \quad (2)$$

The above parameters are explained as follows:

- $H_{j,k}^e$ denotes the channel frequency response (CFR) distortion induced by clock asynchronism, which introduces random phase offsets $\varphi_{j,k}^{\text{TO}}$ (due to TO) and φ_k^{CFO} (due to CFO), varying across subcarriers and CSI packets.
- H_i^h denotes the hardware-related CFR, which captures the effects of RF front-end components, including antennas, cables, circuits, and connectors. *Notably, this term*

may vary across power cycles due to the random initial phase offset introduced by the PLL, which locks the local oscillator to a reference frequency but does not guarantee phase consistency across sessions.

- $H_{i,j}^S$ denotes the CFR contributed by the static paths between the fixed transmitter and receiver, as well as multipath components caused by static environmental clutter. $\rho_{i,j}^S$ is the amplitude of the dominant Tx-Rx path, τ_i^S is its propagation delay, and $\mathbb{H}_{i,j}^S$ accounts for other reflections from surrounding static objects.
- $H_{i,j,k}^X$ denotes the dynamic CFR induced by a moving person. $\rho_{i,j,k}^X$ is the amplitude of the human-reflected path that travels from the transmitter to the human body and then to the receiver, $\tau_{i,k}^X$ is its corresponding propagation delay, and $\mathbb{H}_{i,j,k}^X$ accounts for other dynamic multipath components resulting from human motion.

Hereafter, we consider a coherent processing interval (CPI) consisting of N_t CSI samples within a short-time window. In our work, the CSI sampling frequency is 1 kHz, and we set $N_t = 128$, corresponding to a duration of 0.128 s. Within the short CPI, it is practically reasonable to assume that each moving object's signal amplitude remains constant [9], [23]. In this case, we can further write $H_{i,j}^S$ and $H_{i,j,k}^X$ as

$$\begin{cases} H_{i,j}^S = \rho_{i,j}^S e^{-J2\pi f_j [\tau_i^S + \frac{(i-1)\Delta d}{c} \sin \theta^S]} + \mathbb{H}_{i,j}^S, \\ H_{i,j,k}^X = \rho_{i,j,k}^X e^{-J2\pi f_j [\tau_{i,k}^X + \frac{(i-1)\Delta d}{c} \sin \theta^X + \frac{f^D}{f_c} (k-1)\Delta t]} + \mathbb{H}_{i,j,k}^X, \end{cases} \quad (3)$$

where τ^S and τ^X denote the delay of the Tx-Rx path and the human-reflected path, measured at the first receive antenna at the initial time of the current CPI; θ^S and θ^X are the AoA of the transmitter and human target relative to the Rx antenna array; f^D is the DFS induced by human motion; Δd is the Rx antenna spacing; f_c is the carrier frequency; and Δt is the CSI sampling interval (0.001 seconds).

B. System Overview

This work presents *PowerSense*, a calibration-free and real-time passive tracking system that estimates a subject's position and position-dependent Doppler signatures using CSI power. By discarding phase, the system removes random distortions from hardware imperfections and clock asynchronism, enabling reliable sensing without pre-calibration. Implemented on a commercial LTE prototyping platform with a 1Tx-3Rx bistatic setup, PowerSense jointly extracts delay, AoA, and Doppler features through a lightweight processing pipeline and fuses them for robust trajectory tracking. It further includes a position-guided micro-Doppler module to obtain clear and unambiguous motion signatures. The overall workflow, illustrated in Fig. 1, consists of four main modules:

1) *Random Phase Offset Removal*. Random phase offsets across antennas and time, caused by hardware imperfections and clock asynchronism, are removed by computing CSI power, i.e., multiplying each CSI sample with its complex conjugate. This eliminates all phase distortions while retaining a real-valued, linearly structured signal suitable for extracting delay, AoA, and Doppler features.

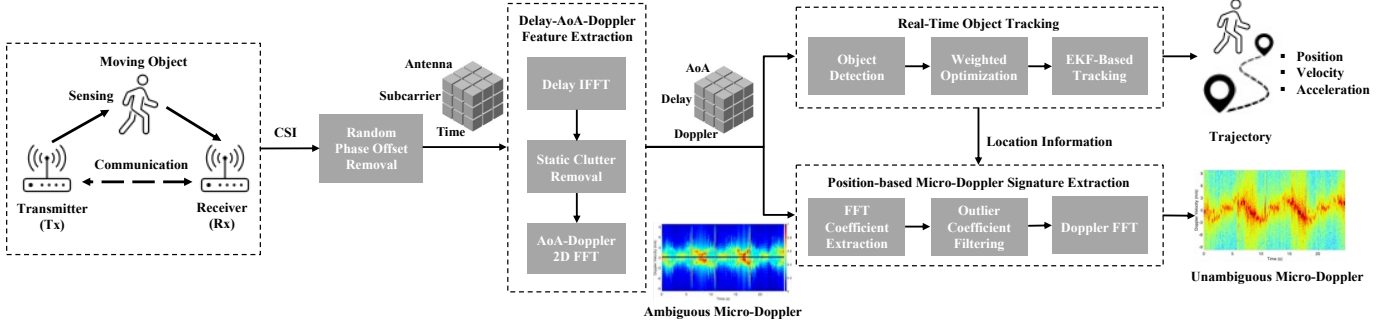


Fig. 1: Overview of the proposed *PowerSense* workflow.

2) *Delay-AoA-Doppler Feature Extraction*. A lightweight cascaded 3D FFT is applied to the CSI power cube (Subcarrier \times Antenna \times Time) to jointly extract delay, AoA, and Doppler. These outputs form a Delay-AoA-Doppler tensor encoding the target's location and motion.

3) *Real-time Passive Tracking*. A CFAR detector identifies valid targets, followed by a weighted joint optimization step for outlier suppression. The filtered delay, AoA, and Doppler features are fused via an EKF to achieve continuous tracking.

4) *Position-based Micro-Doppler Signature Extraction*. The 3D FFT coefficient at the estimated delay-AoA-Doppler peak is selected to isolate body-induced reflections, providing a strong spatiotemporal filter against irrelevant motions. Coefficients across successive CPIs are aggregated and processed by temporal Doppler FFTs to obtain a clean, unambiguous micro-Doppler spectrogram, enabling higher-level behavior sensing.

IV. DELAY-AOA-DOPPLER FEATURE EXTRACTION

This section introduces a lightweight 3D FFT-based pipeline that jointly extracts human motion features from CSI power.

A. Random CSI Phase Offset Removal

Unlike existing methods that explicitly estimate or compensate TO/CFO-induced phase distortions, our approach directly operates on the CSI power, which inherently eliminates all random phase offsets. The distortions introduced by clock asynchronism and hardware imperfections, denoted by $H_{j,k}^e$ and H_i^h , are completely removed when each CSI sample is multiplied by its complex conjugate.

$$\begin{aligned} H_{i,j,k} &= CSI_{i,j,k} \overline{CSI_{i,j,k}} \\ &= H_{j,k}^e H_i^h (H_{i,j}^S + H_{i,j,k}^X) \overline{H_{j,k}^e H_i^h} (\overline{H_{i,j}^S} + \overline{H_{i,j,k}^X}) \\ &= \|H_{j,k}^e H_i^h\|^2 (\|H_{i,j}^S\|^2 + 2\|H_{i,j}^S \overline{H_{i,j,k}^X}\| \cos(\angle H_{i,j}^S \overline{H_{i,j,k}^X}) + \|H_{i,j,k}^X\|^2) \\ &= \|H_{i,j}^S\|^2 + \|H_{i,j,k}^X\|^2 + 2\|H_{i,j}^S \overline{H_{i,j,k}^X}\| \cos(\angle H_{i,j}^S \overline{H_{i,j,k}^X}), \end{aligned} \quad (4)$$

where $\|\cdot\|$ denotes the amplitude; and $\|H_{j,k}^e H_i^h\| = 1$ since both are unit-magnitude exponential terms. According to (2) and (3), we can derive the following expression:

$$\|H_{i,j}^S \overline{H_{i,j,k}^X}\| \cos(\angle H_{i,j}^S \overline{H_{i,j,k}^X}) = \rho_{i,j}^S \rho_{i,j}^X \cos \varphi_{i,j,k} + \Delta \mathbb{H}_{i,j,k}, \quad (5)$$

where

$$\begin{aligned} \varphi_{i,j,k} &= 2\pi f_j (\tau^X - \tau^S) + 2\pi f^D (k-1) \Delta t + \\ &\quad 2\pi f_j \frac{(i-1) \Delta d}{c} (\sin \theta^X - \sin \theta^S). \end{aligned} \quad (6)$$

Here, the delay τ^S and AoA θ^S of the dominant Tx-Rx path are pre-measured values and are considered known constants. The term $\rho_{i,j}^S \rho_{i,j}^X \cos \varphi_{i,j,k}$ is the dominant component while $\Delta \mathbb{H}_{i,j,k}$ is regarded as other multipath contributions.

The key challenges of leveraging CSI power are as follows.

1) *Linear relationship among Delay, AoA, and Doppler*. In Eq. (5), the term $\rho_{i,j}^S \rho_{i,j}^X \cos \varphi_{i,j,k}$ is of our interest, as it captures the interaction between static and dynamic paths and encodes motion-induced variations from the target. This term preserves the inherent linear relationship among delay, AoA, and DFS, which facilitates multi-domain feature extraction.

2) *AoA estimation without calibration*. Existing approaches [8] rely on complex calibration procedures for accurate AoA estimation, which is very challenging for base station arrays due to hardware inconsistencies and deployment constraints. The CSI power method inherently mitigates phase distortions from hardware and clock asynchrony, eliminating the need for complex calibration.

3) *Symmetry-Induced ambiguities in CSI power*. However, the real-valued nature of CSI power introduces inherent symmetry across the delay, AoA, and Doppler domains, making it difficult to distinguish the true target location from its mirrored counterpart. This ambiguity can obscure the interpretation of motion-related features. In this work, we propose a signal processing pipeline to effectively suppress these mirrored components and resolve the ambiguities caused by symmetry.

B. Delay Estimation via IFFT

In our system, each CPI forms a 3D CSI cube of size $N_f \times N_a \times N_t$. The first dimension (spectral) spans N_f subcarriers for delay estimation, the second (spatial) spans N_a receiving antennas for AoA estimation, and the third (temporal) consists of N_t CSI samples for Doppler analysis. We begin by estimating the delay by applying an inverse FFT, denoted as $\mathcal{F}^{-1}(\cdot)$, along the subcarrier dimension. This operation converts the CSI from the frequency domain to the delay domain for each antenna index and time index:

$$\begin{aligned} X_{i,k}[\tau] &= \mathcal{F}_j^{-1}\{H_{i,j,k}\} = \sum_{j=1}^{N_f} H_{i,j,k} \cdot e^{j2\pi f_j \tau} \\ &= \sum_{j=1}^{N_f} \left[(\rho_{i,j}^S)^2 + (\rho_{i,j}^X)^2 \right] e^{j2\pi f_j \tau} + \\ &\quad \sum_{j=1}^{N_f} \frac{1}{2} \rho_{i,j}^S \rho_{i,j}^X (e^{j\varphi_{i,j,k}} + e^{-j\varphi_{i,j,k}}) e^{j2\pi f_j \tau} + \Delta \mathcal{N}_{i,k}, \end{aligned} \quad (7)$$

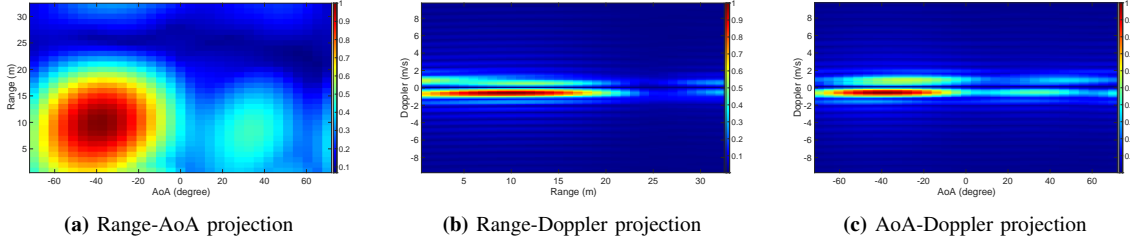


Fig. 2: Three 2D projections of the 3D Range-AoA-Doppler tensor along different dimensions.

where τ denotes the delay bin. For cases involving non-uniform subcarrier spacing, interpolation can be applied, or alternatively, a non-uniform FFT can be directly used to improve efficiency. The term $\Delta\mathcal{N}_{i,k}$ represents other reflections that remain in the delay domain after the IFFT.

By applying the delay IFFT, the CSI power is decomposed into multiple delay bins. Because the IFFT of a real-valued sequence yields symmetric spectral components, we retain only the single-sided spectrum by selecting $\tau > 0$, which suppresses mirrored artifacts arising from spectral symmetry. Ideally, with only a static Line-of-Sight (LOS) path present, human-induced reflections always exhibit longer propagation delays than the direct LOS path, and thus the positive-delay bins (i.e., $\tau^X - \tau^S > 0$) correspond to physically meaningful motions. In practice, however, indoor environments contain numerous static reflectors. Some static multipath components may experience propagation delays comparable to or even longer than the human-reflection path, meaning that paths with $\tau^X - \tau^S < 0$ can also be physically valid. These negative-delay components fold onto the positive side due to spectral mirroring in the real-valued IFFT output and may introduce additional interference. Moreover, the limited bandwidth in ISAC systems restricts delay resolution, making it challenging to separate closely spaced multipath components. Subsequent AoA and Doppler processing can effectively mitigate these interferences and the remaining contributions.

C. Static Clutter Removal

To highlight motion-related signals, static clutter is removed from each delay bin by subtracting the average over the CPI:

$$\tilde{X}_{i,k}[\tau] = X_{i,k}[\tau] - \frac{1}{N_t} \sum_{k=1}^{N_t} X_{i,k}[\tau]. \quad (8)$$

After delay-domain IFFT, static reflections are dispersed across delay bins. This averaging approach effectively suppresses them, while the resulting signal $\tilde{X}_{i,k}[\tau]$ emphasizes dynamic paths, facilitating more accurate Doppler and AoA estimation in subsequent steps. As a simple extension to the proposed processing framework, high resolution nullifying filters with a deep and narrow null at the zero frequency can be designed and applied for removing static clutter [24], which is beyond the focus of this work.

D. AoA-Doppler Estimation via 2D FFT

For each delay bin τ , we estimate the target's AoA and DFS by applying a 2D FFT along the spatial and temporal dimensions, respectively. Prior to the transform, we apply

phase compensation with respect to the known transmitter angle θ^S to align the dynamic reflections for target AoA estimation. The compensated signal is defined as:

$$X'_{i,k}[\tau] = \tilde{X}_{i,k}[\tau] e^{j2\pi \frac{(i-1)\Delta d}{\lambda} \sin \theta^S}. \quad (9)$$

The AoA-Doppler spectrum is computed via a 2D FFT as:

$$\begin{aligned} Y[\tau, \theta^X, f^D] &= \mathcal{F}_{i,k} \{X'_{i,k}[\tau]\} \\ &= \sum_{i=1}^{N_a} \sum_{k=1}^{N_t} X'_{i,k}[\tau] \cdot e^{j2\pi \left(\frac{(i-1)\Delta d}{\lambda} \sin \theta^X + f^D (k-1)\Delta t \right)} + \Delta\mathbb{N}. \end{aligned} \quad (10)$$

The following notes are made for the above result.

- $\Delta\mathbb{N}$ represents residual components arising from secondary reflections and mirrored artifacts introduced by the IFFT of real-valued CSI power.
- Each AoA bin can be mapped to a physical angle based on the array geometry. For an N_θ -point spatial FFT, the angle corresponding to the n -th bin is given by:

$$\theta^X = \arcsin \left[\frac{\lambda}{\Delta d} \left(\frac{n}{N_\theta} - 0.5 \right) \right], \quad (11)$$

where $n \in [0, N_\theta - 1]$ is the FFT bin index, and λ is the signal wavelength. For example, with $\Delta d = \lambda/2$, the FFT output spans an angular range of $[-90^\circ, +90^\circ]$. Since the transmitter is fixed and its direction θ^S is known, the AoA θ^X is expected to lie within a limited sector.

- The estimated Doppler frequency f^D can be converted into Doppler velocity using:

$$v^D = \frac{cf^D}{f_c}. \quad (12)$$

We assume that indoor human motion typically lies within a velocity range of ± 5 m/s, allowing us to constrain the Doppler to the corresponding frequency band.

Finally, by repeating the AoA-Doppler estimation process across all delay bins, we can construct a 3D Delay-AoA-Doppler feature tensor $Y[\tau, \theta^X, f^D] \in \mathbb{C}^{N_\tau \times N_\theta \times N_f}$, where N_τ , N_θ , and N_f denote the number of delay, AoA, and Doppler bins, respectively. This tensor offers a comprehensive representation of human motion dynamics. The joint exploitation of the AoA and Doppler domains further enhances dominant motion components while suppressing weak or irrelevant reflections. This is because human-induced reflections typically exhibit coherent energy concentrated at specific angles and Doppler frequencies, whereas non-target reflections are often dispersed and lack consistent spatial-temporal signatures. In this case, when a moving target is present, the dominant reflection typically appears as a peak in the 3D tensor. By

identifying the maximum energy point, we can estimate the target's parameters as:

$$\arg \max_{\tau, \theta^X, f^D} \|Y[\tau, \theta^X, f^D]\|. \quad (13)$$

As shown in Fig. 2, we visualize three 2D projections of the constructed 3D Delay-AoA-Doppler tensor based on 3.1 GHz LTE signals to intuitively illustrate motion features across different dimensions. (1) *Range-AoA Projection* reveals the spatial distribution of the target, where the reflection appears as a concentrated energy cluster (highlighted in red) at a specific delay and angle. Due to the limited resolution resulting from the 20 MHz bandwidth and the use of a 3-element linear Rx antenna array, the cluster appears spatially spread, forming a broad lobe across the delay and angular dimensions. (2) *Range-Doppler* and *AoA-Doppler Projections* capture the target's radial motion characteristics along the delay and angle dimensions, respectively. Compared to the delay and AoA, the Doppler exhibits a narrower lobe, indicating higher resolution in Doppler estimation. The red region corresponds to the target's actual position and motion-induced DFS. However, we also observe a weaker symmetric component on the opposite Doppler side, caused by mirrored artifacts. While selecting the peak Delay-AoA-Doppler bin enables accurate object tracking, the presence of mirrored components can introduce ambiguity in more fine-grained applications such as activity recognition. This issue is further addressed in Section VI.

E. Feature Extraction Complexity

As defined above, N_τ , N_θ , and N_f denote the number of FFT bins along the spectral (delay), spatial (AoA), and temporal (Doppler) dimensions, respectively. The overall complexity of the 3D FFT-based feature extraction is $\mathcal{O}(N_\tau N_\theta N_f \log N)$, where $N = \max(N_\tau, N_\theta, N_f)$. Due to the FFT's efficiency and the modest bin sizes involved (e.g., $N_\tau = 128$, $N_\theta = 32$, $N_f = 128$), the computation remains lightweight and is well-suited for real-time implementation, even potentially on edge devices with limited computational resources.

V. PASSIVE OBJECT DETECTION AND TRACKING

This section presents a real-time object detection and tracking framework to continuously track human positions.

A. Subcube-Based Object Detection

In conventional CFAR algorithms commonly used in radar systems [25], a detection window is defined around a test cell, separated by guard cells and surrounding reference cells. The energy in the reference cells is used to estimate the local noise floor for thresholding. However, in our bistatic system, residual mirrored components may contaminate the guard and reference regions. If the guard cells include mirrored interference, the resulting noise estimate will be biased. Instead, we adopt the following subcube-based approach.

We begin by identifying the global peak within the extracted 3D Delay-AoA-Doppler tensor, and recording its amplitude and corresponding indices. We then define a small cubic region (called subcube) centered at the peak location with a size of

$3 \times 3 \times 3$ bins to capture the local energy distribution. The average energy within this subcube, denoted as P_{subcube} , is computed and then compared against the global noise floor, defined as the average energy across the entire tensor P_{noise} . The object is considered a valid detection if the energy ratio satisfies the following condition:

$$\text{SNR} = \frac{P_{\text{subcube}}}{P_{\text{noise}}} > \alpha, \quad (14)$$

where α is a predefined detection threshold. If this condition is met, the corresponding target parameters, including delay, AoA, DFS, and SNR, are extracted for subsequent tracking. Otherwise, the detection is discarded to suppress false alarms.

B. Weighted Joint Optimization

In human sensing, signals first interact with the human body and are then reflected to the receiver through diffuse scattering. Due to body motion, the reflected signals may become unstable at certain times, resulting in outliers. Moreover, although mirrored components are largely suppressed through the above step, their residual interference along with the inherently low resolution and high noise levels, particularly in delay and AoA estimates, further exacerbates the occurrence of such outliers. These anomalies significantly degrade the accuracy and stability of the subsequent EKF-based tracking process.

1) *Outlier Filtering*. To address this, we adopt a robust weighted joint optimization approach that fuses the estimated signal parameters across multiple adjacent CPIs. Due to the low computational cost of our system (less than 2 ms per CPI, as shown in Section VII), we can aggregate a large number of estimates within a time window. For instance, a 1-second optimization window contains up to 500 parameter estimates, which provides sufficient redundancy to suppress outliers. Before computing the weighted average, we apply a statistical outlier removal method based on the Z-score criterion to filter out abnormally deviated estimates. Given a set of parameter estimates R_l (Delay, AoA, Doppler and SNR), the Z-score of the l -th estimate is computed as:

$$Q_l = \frac{R_l - \mu_R}{\sigma_R}, \quad (15)$$

where μ_R and σ_R denote the mean and standard deviation of the corresponding parameter. Any estimate satisfying

$$|Q_l| > \delta_Q \quad (16)$$

is regarded as an outlier and removed from the set. We adopt a threshold of $\delta_Q = 3.0$ for all parameter dimensions (Delay, AoA, Doppler, and SNR), following the well-known three-sigma rule, which retains 99.7% of samples under a Gaussian distribution while removing statistically significant outliers.

2) *Weighted Optimization*. The remaining estimates are then combined using the estimated SNR as a weighting factor. The refined value of a parameter P (where P represents Delay, AoA, or DFS) is computed as

$$P_{\text{weighted}} = \frac{\sum_l \text{SNR}_l P_l}{\sum_l \text{SNR}_l}, \quad (17)$$

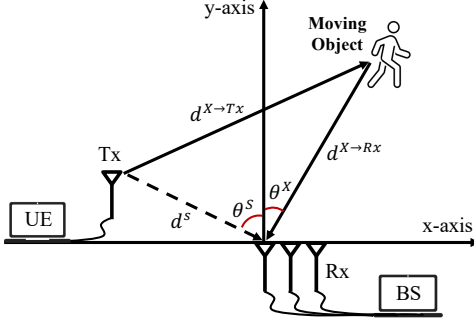


Fig. 3: Geometry of bistatic LTE system for passive object tracking.

where P_l denotes each estimated parameter, and SNR_l is the corresponding SNR in dB. This prioritizes high-quality measurements, reducing the impact of noise and improving tracking accuracy and stability before applying EKF.

C. Object Tracking via EKF

We next employ an EKF to estimate the target's position, velocity, and acceleration over time.

1) *Coordinate Transformation.* As shown in Fig. 3, the detected delay and AoA are converted into Cartesian coordinates for EKF input. In a bistatic sensing system, the target-to-receiver distance can be computed as

$$d^{X \rightarrow RX} = \frac{(d^X)^2 - (d^S)^2}{2[d^X - d^S \cos(\theta^X - \theta^S)]}, \quad (18)$$

where $d^X = \tau^X c$ is the estimated reflection range; d^S is the known Tx-Rx distance; θ^X and θ^S are the AoAs of the target and transmitter, respectively. The Cartesian coordinates are then derived as:

$$\begin{cases} x = d^{X \rightarrow RX} \sin \theta^X, \\ y = d^{X \rightarrow RX} \cos \theta^X. \end{cases} \quad (19)$$

2) *EKF-based Tracking.* Each valid detection initializes a six-dimensional state vector $[x, y, v_x, v_y, a_x, a_y]^T$, where the position (x, y) is computed from the estimated delay and AoA. The initial velocity (v_x, v_y) is set to half the Doppler-derived velocity, while acceleration components (a_x, a_y) are initialized to a small constant (e.g., 0.1 m/s^2). The EKF then iteratively predicts the target's state using a constant-acceleration model and compares incoming measurements via Euclidean distance. If the measurement falls within a distance threshold, it updates the state with the observed position and Doppler velocity; otherwise, the track is temporarily retained. If no valid measurement is associated for a predefined number of consecutive frames (e.g., 20 frames), the track is removed.

VI. POSITION-BASED MICRO-DOPPLER EXTRACTION

Micro-Doppler [26]–[29] refers to the fine-grained Doppler modulations induced by micro-motions, such as swinging arms or legs. These subtle and often periodic signatures are highly informative for tasks like activity recognition [30], [31] and individual identification [32]. In passive sensing, micro-Doppler features provide valuable cues for inferring the subject's motion type, activity state, or intent. However, the

Doppler domain suffers from mirrored components due to the use of real-valued CSI power. Although mirror suppression is performed in the above steps, residual ambiguity still persists along the Doppler dimension. To address this, we extract unambiguous micro-Doppler signatures by leveraging the target's location, as shown in Fig. 4.

1) *3D FFT Coefficient Extraction.* For each CPI, we identify the dominant motion component by selecting the peak energy bin in the 3D Delay-AoA-Doppler tensor. The peak index is determined as $\{\tau^*, (\theta^X)^*, (f^D)^*\}$, so the extracted 3D FFT coefficient $Z_t = Y[\tau^*, (\theta^X)^*, (f^D)^*]$ represents the filtered CSI signal at time t , associated with the dominant motion path.

Due to the real-valued nature of CSI power and limited resolution in the delay and AoA domains, multiple micro-motions from different body parts may overlap, and mirrored Doppler components still persist in Z_t . Let f^D denote the dominant Doppler shift and $-f^D$ its mirrored counterpart. Due to the selective filtering effect of the 3D FFT, mirrored components carry weaker energy due to delay-domain filtering, i.e., $\rho[l] > \rho'[l]$. In this case, the extracted coefficient Z_t is modeled as a superposition of multiple micro-Doppler components:

$$Z_t = \sum_l \left[\rho[l] e^{j(2\pi f^D[l]t + \phi[l])} + \rho'[l] e^{-j(2\pi f^D[l]t + \phi'[l])} \right], \quad (20)$$

where each term represents a dynamic reflection from a moving body part, characterized by amplitude $\rho[l]$, Doppler frequency $f^D[l]$, and initial phase $\phi[l]$. This complex-valued sequence $\{Z_t\}$ is then used in subsequent Doppler-time analysis to extract fine-grained motion signatures without ambiguity.

2) *Outlier Frame Processing.* As discussed in Section V.B, we employ a weighted joint optimization framework to suppress parameter outliers, using a Z-score-based criterion for detection and removal. Consequently, certain CPIs are marked invalid, resulting in missing values in the Doppler processing chain. We apply temporal interpolation to restore these gaps. We then segment the complex-valued 3D FFT coefficients using a sliding window approach. Specifically, each temporal window $\mathbf{S}_t = \{Z_t, Z_{t+1}, \dots, Z_{t+L-1}\}$ consists of L consecutive FFT coefficients centered around the estimated target location (in delay and AoA). A stride of 2 samples is used, balancing resolution and efficiency. Thanks to our lightweight processing pipeline (under 2 ms per CPI at 1 kHz, as detailed in Section VII.B), this dense slicing supports high-resolution Doppler extraction.

3) *Unambiguous Doppler Construction.* To capture fine-grained motion dynamics, we perform a 1D Doppler FFT across each temporal window \mathbf{S}_t , yielding:

$$\mathcal{Z}_t[f^D] = \sum_{k=1}^L Z_{t+k-1} \cdot e^{-j2\pi f^D(k-1)\Delta t'}, \quad (21)$$

where $\Delta t'$ is the CSI sampling interval (2 ms). This localized Doppler spectrum $\mathcal{Z}_t[f^D]$ reflects the target's motion within each window while mitigating mirrored Doppler artifacts.

By sliding the window across time, we construct a continuous Doppler-time spectrogram that robustly captures micro-motion signatures. The resulting representation highlights periodic limb movements from different body parts, offering

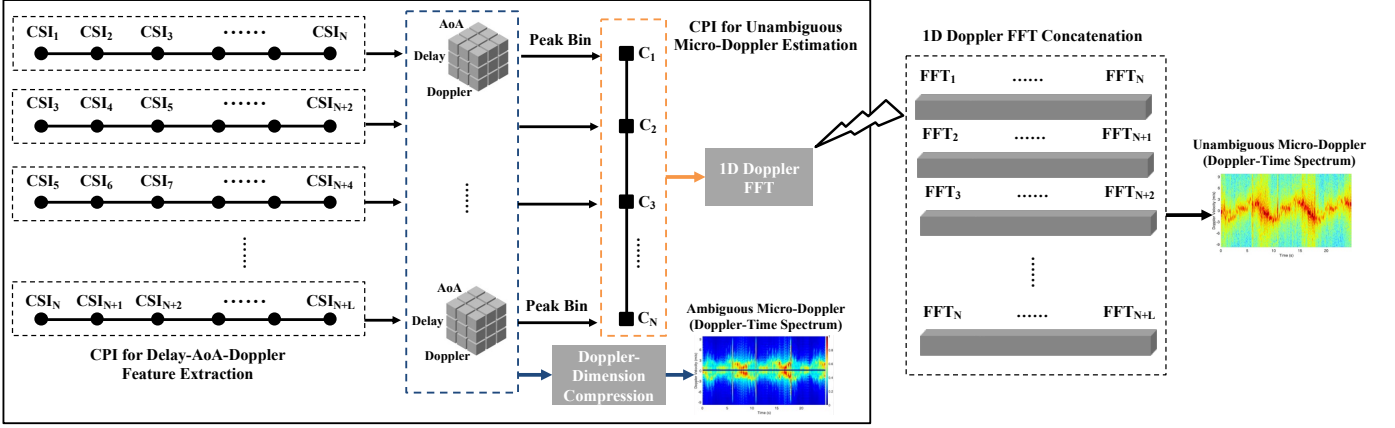


Fig. 4: Pipeline for constructing unambiguous micro-Doppler signatures.

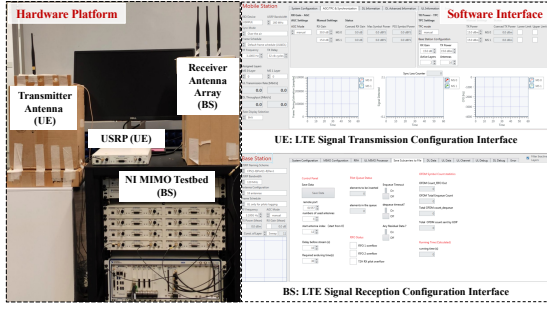


Fig. 5: Testbed and software interface for LTE CSI collection.

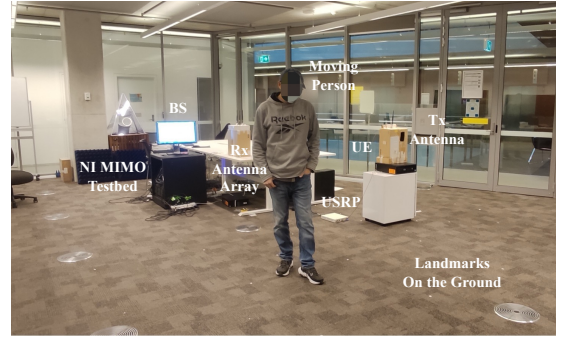


Fig. 6: Experiment scenario.

rich cues for downstream behavior understanding. This work focuses on extracting high-quality micro-Doppler features in bistatic passive systems. Future work will explore their use in activity classification via deep learning.

VII. EXPERIMENTAL RESULTS

This section presents a comprehensive evaluation of PowerSense's performance through extensive experiments.

A. CSI Acquisition

This work primarily evaluates tracking performance using an 3.1 GHz LTE-based CSI extraction platform [33], while additional experiments on 5 GHz WiFi CSI are also conducted to validate the proposed micro-Doppler extraction quality.

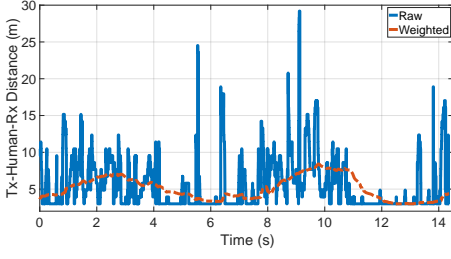
1) *LTE System Setup.* As shown in Fig. 5, the platform comprises an NI Massive MIMO prototyping testbed functioning as the BS and a USRP device acting as the UE. The BS is equipped with a linear array of three antennas, while the UE has a single antenna. The uplink CSI is extracted at the BS based on pilot signals transmitted from the UE.

2) *LTE Pilot Signals.* The system adopts the standard 3GPP LTE frame structure. Each LTE frame spans 10 ms and consists of 10 subframes (1 ms each), with each subframe divided into two 0.5 ms slots. Within each slot, uplink transmission is organized into 7 OFDM symbols, each lasting approximately 66.67 μ s. Pilot signals are transmitted once per slot. Each pilot sequence comprises 1200 QPSK-modulated symbols, mapped to 1200 subcarriers spaced at 15 kHz, covering a

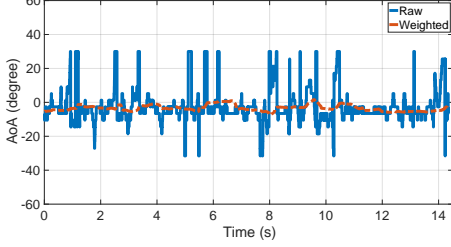
20 MHz bandwidth. Each resource block (RB) includes 12 consecutive subcarriers, totaling 180 kHz in bandwidth. Thus, the 1200 subcarriers form 100 RBs, with each spatial layer mapped to one subcarrier per RB, supporting up to 12 spatial layers. In our system, only the first spatial layer is active, so one subcarrier per RB is modulated with a pilot, and the remaining subcarriers are padded with nulls. This results in 100 pilot-bearing subcarriers out of 1200, all of which are transmitted. During CSI extraction, we focus on these 100 active subcarriers. Since there is one pilot per RB, the effective subcarrier spacing becomes 180 kHz, reflecting RB-level resolution rather than the original 15 kHz subcarrier grid.

3) *LTE CSI Extraction.* We implement a pilot-streaming interface using LabVIEW Communications 2.0, integrated with the Massive MIMO Framework Application (MMFA). The interface filters out unused subcarriers and selects valid pilots to reduce data throughput. The CSI sampling rate is downsampled from 2 kHz to 1 kHz to mitigate packet loss during UDP transmission. The extracted CSI is streamed to the host computer in real time for passive tracking tasks.

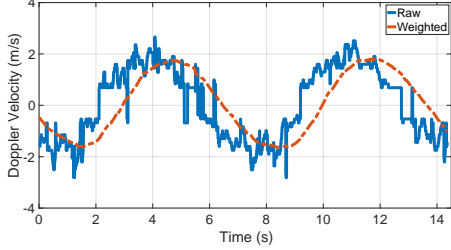
To assess the generalizability of the proposed PowerSense beyond LTE signals, we further apply the proposed micro-Doppler extraction module to 5 GHz WiFi CSI measurements from the public GaitID dataset [34]. The dataset contains CSI recordings of human walking motions collected from multiple subjects using a commercial WiFi transceiver in a bistatic setup, enabling cross-platform validation of micro-Doppler clarity and robustness.



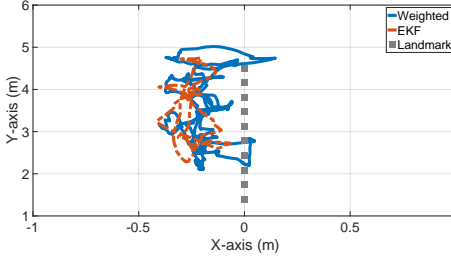
(a) Range



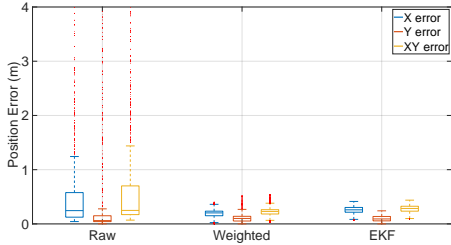
(b) AoA



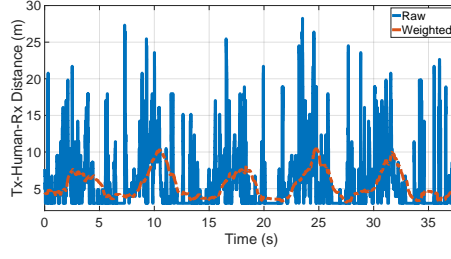
(c) Doppler



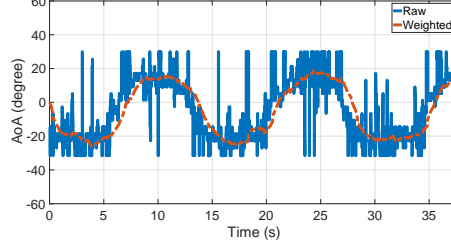
(d) Estimated trajectory



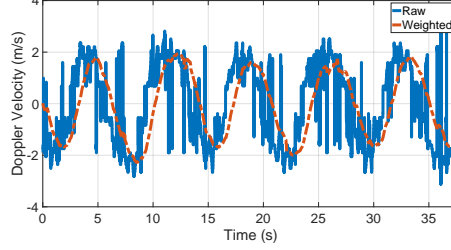
(e) Position error

Fig. 7: Linear trajectory.

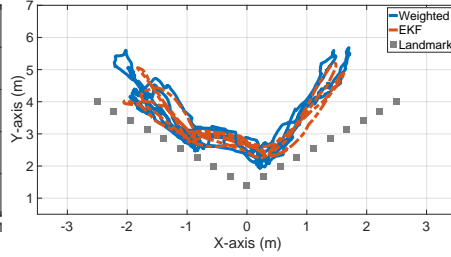
(a) Range



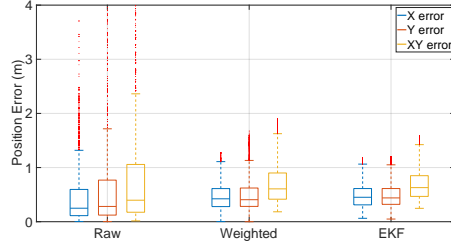
(b) AoA



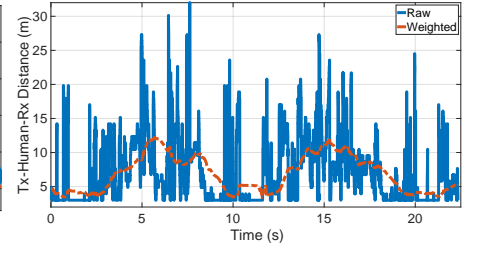
(c) Doppler



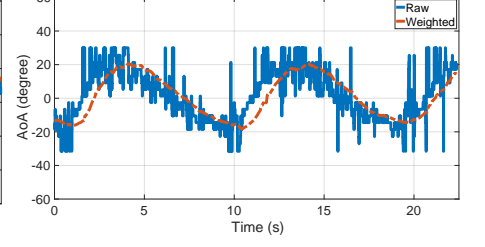
(d) Estimated trajectory



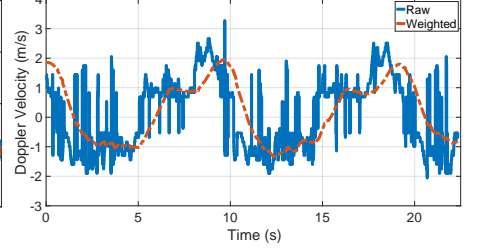
(e) Position error

Fig. 8: V-shaped trajectory.

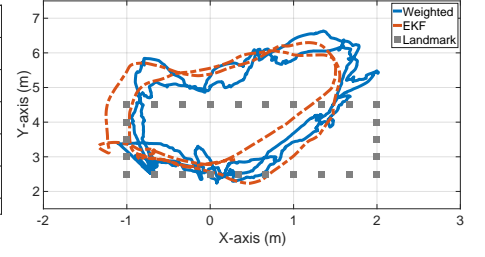
(a) Range



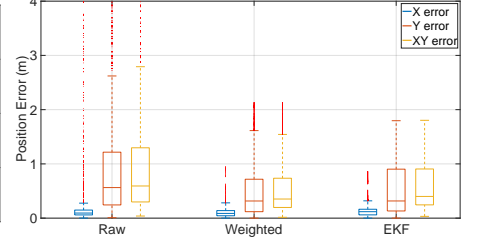
(b) AoA



(c) Doppler



(d) Estimated trajectory



(e) Position error

Fig. 9: Rectangular trajectory.

B. Implementation

1) *LTE and WiFi CSI*. As detailed above, the LTE CSI is collected at 3.1 GHz using 100 subcarriers and 3 Rx antennas, with a CSI sampling rate of 1 kHz. Each CSI sample forms a 100×3 matrix and is streamed via UDP to a host PC for real-time processing. In addition, WiFi CSI is obtained from the GaitID dataset using an Intel 5300 NIC operating at 5 GHz over a 20 MHz channel, providing 30-subcarrier CSI per packet across three receiving antennas.

2) *Motion Trajectory*. As shown in Fig. 6, the experiments

are conducted in a lab environment containing typical indoor objects such as monitors, desks, and chairs. A person walks along three trajectories at a nominal speed of 1 m/s: *a straight line, a V-shaped path, and a rectangular path*. These trajectories are marked on the floor to serve as ground truth.

3) *CPI and FFT Configuration*. Each CPI contains 128 CSI samples across 100 subcarriers and 3 Rx antennas, forming a $100 \times 3 \times 128$ tensor. The delay, AoA, and Doppler FFT bin sizes are 128, 32, and 128, respectively. On our platform (2019 MacBook Pro with a 2.6 GHz 6-core Intel Core i7 pro-

TABLE I: Median errors along the X and Y axes for different trajectories based on Delay-AoA-Doppler joint estimation (m).

Method	Linear		V-shape		Rectangle	
	X	Y	X	Y	X	Y
Our CSI Power	0.25	0.09	0.45	0.42	0.11	0.31
DCACC [8], [9], [33]	0.07	0.29	0.28	0.30	0.22	0.76

cessor), the average processing time per CPI is less than 2 ms (evaluated in Section VII.E). To enable real-time processing, a step size of 2 samples can be used, resulting in an overlap of 126 samples between adjacent CPIs. The selected 64 3D FFT peaks from each CPI are processed using a 128-point Doppler FFT over time to construct micro-Doppler signatures.

4) *CFAR-based Detector and Weighted Optimization.* CFAR detection uses a $3 \times 3 \times 3$ cubic window, with a threshold of 5 for valid detection (see Section VII.D). For weighted optimization, a 1.5-second sliding window aggregates recent CPI outputs to filter outliers.

5) *EKF Tracker.* A detection is associated with a track if its Euclidean distance to the predicted position is within 2 m. A track is confirmed when it persists for more than 20 frames with a visibility ratio above 0.6 and fewer than 5 consecutive missed detections; otherwise, it is removed. Tracks younger than 20 frames remain for further evaluation.

6) *Tracking Performance Comparison.* For a fair comparison, we mainly evaluate the proposed PowerSense against representative Delay-AoA-Doppler joint estimation methods [8], [9], [33], which employ improved antenna-pair conjugation to mitigate clock asynchrony but still require prior antenna calibration for accurate AoA estimation. Unlike these more advanced methods that utilize all three signal dimensions, JUMP [11] performs localization using only delay and AoA without incorporating Doppler information, while Widar 2.0 [7] requires an accurate initial target position to initialize its maximum-likelihood estimator. Given these differences, they are not included in the subsequent evaluations.

7) *Micro-Doppler Quality Comparison.* We assess the quality of the micro-Doppler signatures against three baselines: Raw CACC [7], DCACC [8], [9], and CASR [21]. We also validate our method in a single-antenna setting using only delay and Doppler processing, without requiring spatial diversity.

C. Overall tracking performance

We evaluate the proposed *PowerSense* on three trajectories. Fig.7, Fig.8, and Fig.9 show the Delay, AoA, and Doppler features, along with the weighted and EKF-refined trajectories.

1) First, due to the limited bandwidth (20 MHz), the delay (range) estimates exhibit higher noise than those in the AoA and Doppler domains. Second, the weighted optimization method suppresses outliers by aggregating information over a 1.5-second window, though this introduces a fixed processing delay. Third, EKF refinement produces smoother and more coherent trajectories than the weighted features alone.

2) Fig.7 (c)–Fig.9 (c) show that the 3D FFT mitigates mirrored components, particularly in the Doppler domain, where raw real-valued Doppler features exhibit symmetric ambiguities that are notably suppressed in our results.

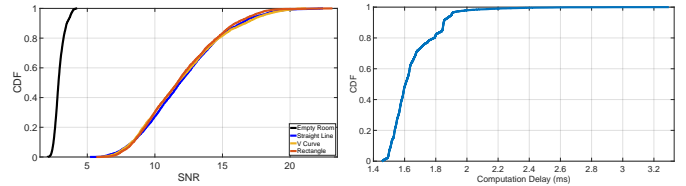


Fig. 10: Detection threshold.

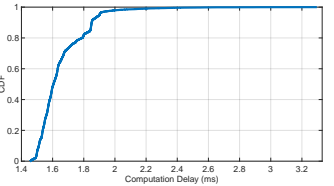


Fig. 11: Computation delay.

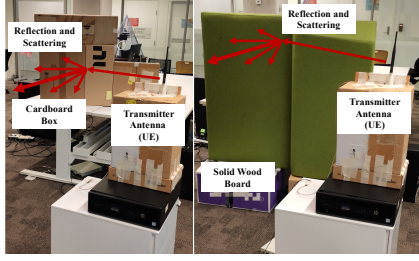
3) Fig.7 (e)–Fig.9 (e) illustrate the tracking accuracy using error bars along the X-, Y-, and combined XY-axes. We can see that the average EKF tracking errors in the XY-plane for the linear, V-shaped, and rectangular trajectories are 0.28 m, 0.68 m, and 0.60 m, respectively, with an overall average of 0.52 m. The errors along the X-axis are typically smaller than those along the Y-axis, which can be attributed to the geometric configuration of the transmitter and receiver.

D. Tracking accuracy comparison

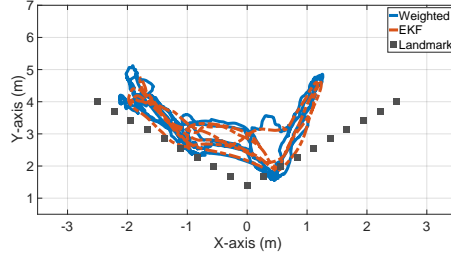
We compare the proposed *PowerSense* with a DCACC-based method [8], [9], [33]. Due to occasional outlier estimates in the baseline, the associated Kalman filter updates may become unstable. As a result, the works reports *median* tracking errors instead of mean values. To ensure a fair comparison, we adopt the same median error metric. Table I summarizes the tracking accuracy along the X and Y axes for both methods. Our *PowerSense* achieves a median XY tracking error of 0.4 m, compared to 0.50 m for the baseline methods, representing an improvement of about 10 cm. The overall tracking accuracy of the two approaches is relatively close. Importantly, the baseline relies on accurate antenna array calibration, which must be repeated each time the system is restarted due to hardware-induced phase variations. In contrast, our approach mitigates such inconsistencies by leveraging CSI power, eliminating the need for any pre-calibration. Furthermore, our lightweight signal processing pipeline significantly reduces computational overhead, allowing more data points to be jointly optimized for outlier suppression and noise smoothing. Overall, *PowerSense* provides a robust, calibration-free solution for real-time passive tracking with improved accuracy and practicality.

E. Object detection accuracy

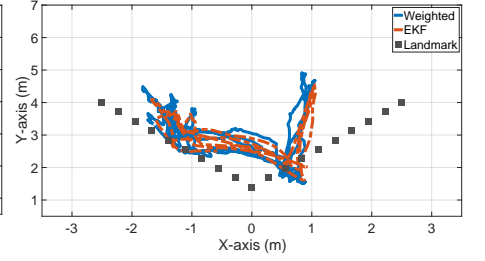
We evaluate the performance of the proposed CFAR-based detection method under static and dynamic conditions by analyzing the cumulative distribution function (CDF) of measured SNR values, as shown in Fig. 10. In static environments (e.g., an empty room), the SNR values remain consistently low, with over all of the samples falling below the detection threshold of 5 dB. This confirms that static clutter rarely exceeds the decision threshold, effectively minimizing false alarms. In contrast, dynamic scenarios involving human motion exhibit higher SNRs. In all motion trajectories tested (straight, rectangle, V-curve), all of SNR values exceed the 5 dB threshold, enabling robust target detection. Since our method adopts a self-adaptive CFAR strategy, a fixed threshold can be uniformly applied across varying environments. These results demonstrate the effectiveness of the CFAR-based detector in suppressing false alarms under static conditions while maintaining high detection sensitivity in dynamic scenarios.



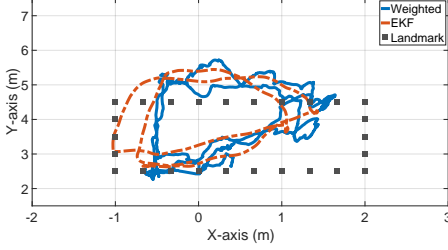
(a) NLOS setups.



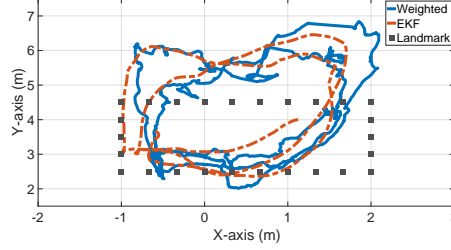
(b) Hard cardboard box.



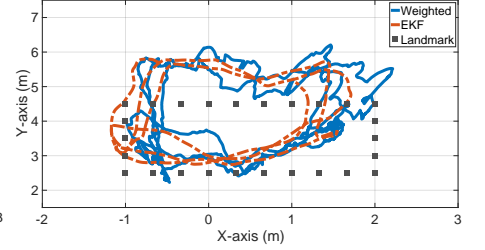
(c) Solid wood board

Fig. 12: Impact of NLOS scenarios.

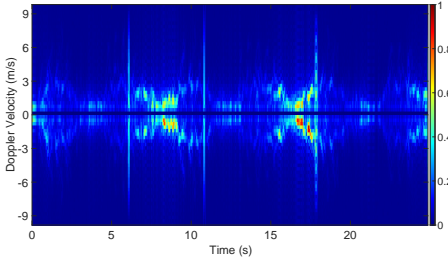
(a) High-speed movement (1.2 m/s)



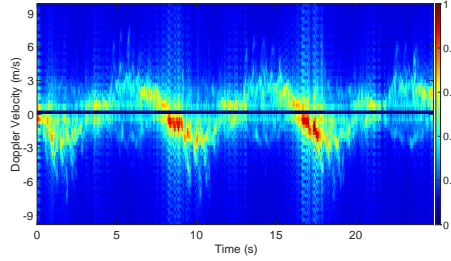
(b) Medium-speed movement (1.0 m/s)



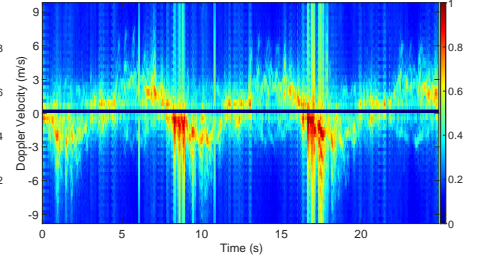
(c) Low-speed movement (0.7 m/s)

Fig. 13: Impact of moving speed.

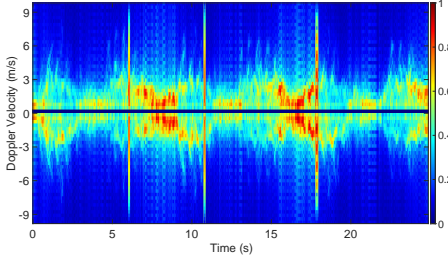
(a) Raw CACC



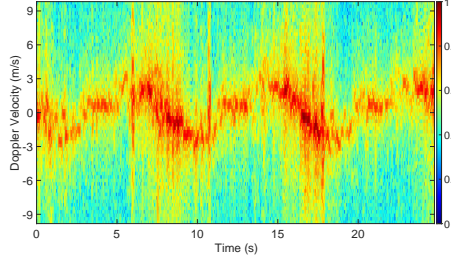
(b) DCACC



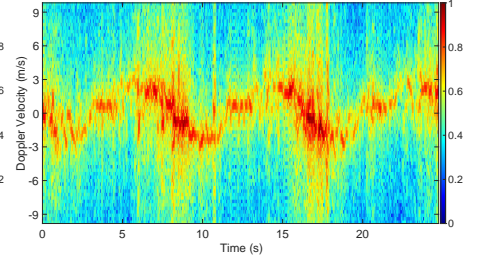
(c) CASR



(d) Ours (3D FFT tensor)



(e) Ours (multi-antenna)



(f) Ours (single-antenna)

Fig. 14: Comparison of micro-Doppler spectrums for different methods during human motion along a rectangular trajectory.

F. Real-time performance

We evaluate the real-time performance using the CDF of computation delay per CPI in Fig. 11. On our platform, the average processing time per CPI (128 CSI samples) is 1.65 ms, and over 98% of frames are completed within 1.93 ms. This high computational efficiency is attributed to the lightweight FFT-based feature extraction pipeline and the linear complexity of the tracking module. The fast processing enables the use of a larger temporal window for improved outlier suppression. Moreover, it enables a small step size of 2 CSI samples (i.e., 2 ms), facilitating dense temporal sampling and achieving unambiguous micro-Doppler extraction. Overall, the entire processing chain satisfies real-time requirements without relying on dedicated hardware acceleration.

G. Impact of NLOS scenarios

To assess the performance of PowerSense under non-line-of-sight (NLOS) conditions, we introduce controlled obstructions near the transmitter using two types of obstacles: a cardboard box and a solid wood board, as illustrated in Fig. 12(a). The corresponding tracking results are presented in Fig. 12(b) and (c). Compared with the LOS trajectory in Fig. 8(d), the estimated paths under both NLOS conditions show increased deviations from the ground truth. The solid wood board results in noticeably larger errors than the cardboard box, likely due to its stronger reflective surface. These observations indicate that pronounced multipath in NLOS environments can degrade delay and AoA estimation, thereby affecting overall tracking accuracy.

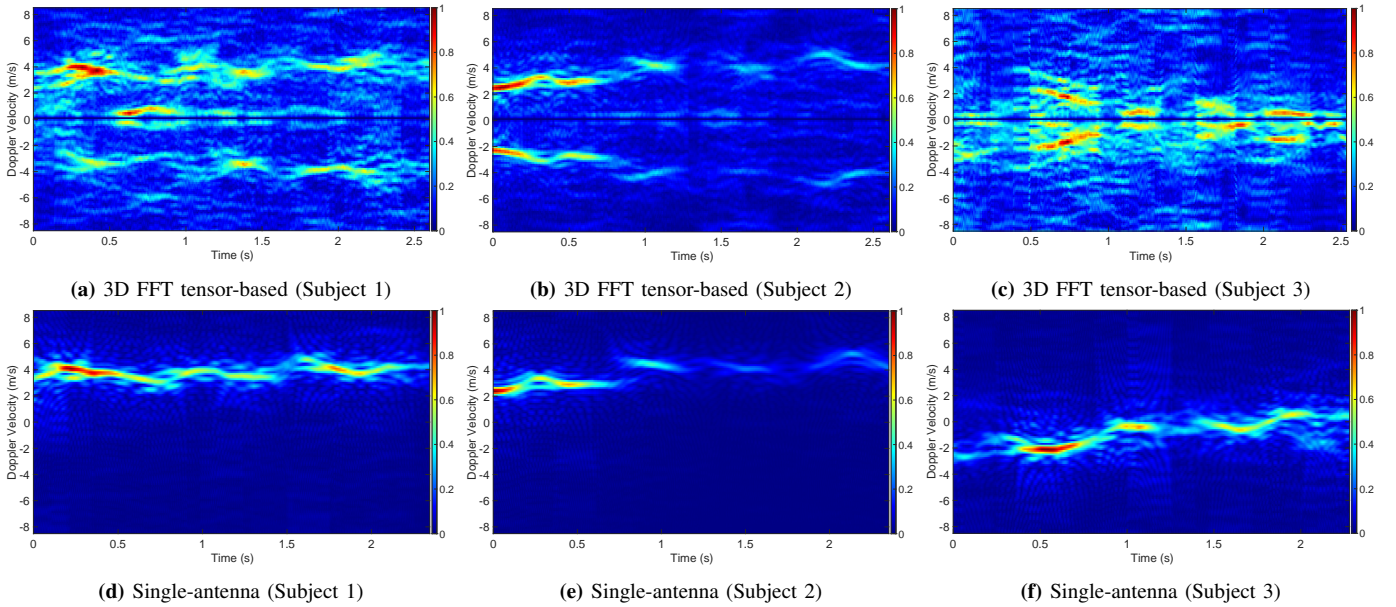


Fig. 15: Micro-Doppler signatures of human gait extracted from WiFi signals for three different subjects using the same receiver.

H. Impact of movement velocity

Fig. 13(a)–(c) compare tracking results at different walking speeds: fast (1.2 m/s), medium (1.0 m/s), and slow (0.7 m/s). In all cases, PowerSense yields smooth and continuous trajectories that generally align with the ground truth. Interestingly, faster motion does not lead to higher tracking accuracy, which aligns with findings in [8]. Faster movement produces larger Doppler shifts, making the target more distinguishable. However, practical challenges such as unstable scattering from rapidly moving body parts and increased signal fluctuations may offset this advantage, leading to reduced performance.

I. Micro-Doppler quality

To ensure consistent comparison, the extracted micro-Doppler signatures are log-transformed and normalized to the range [0, 1]. We evaluate the Doppler quality using uplink CSI data collected along a rectangular trajectory, comparing six methods: Raw CACC [7], DCACC [8], [9], CASR [21], and our proposed 3D tensor, multi-antenna, and single-antenna approaches. Specifically, the 3D tensor method compresses the Delay-AoA-Doppler cube into a 1D Doppler profile per CPI. The multi-antenna method leverages full 3D FFT processing, while the single-antenna method applies only delay and Doppler filtering, without spatial (AoA) processing.

As shown in Fig. 14, the raw CACC method suffers from strong mirrored components, leading to ambiguous Doppler. Both the DCACC and CASR methods reduce these artifacts, with DCACC offering better temporal stability. However, DCACC requires three Rx antennas, and its use of CSI-ratio introduces nonlinear distortions that complicate delay and AoA estimation. By comparison, our 3D tensor method still exhibits mirrored components similar to raw CACC. In contrast, the multi-antenna and single-antenna variants of our approach significantly suppress mirrored artifacts, producing clearer and unambiguous Doppler profiles. Notably, the single-antenna method achieves comparable performance using only

delay and Doppler filtering, demonstrating its potential for low-complexity deployment.

J. Extension beyond LTE signals

To validate the generalizability of our approach, we apply it to 5 GHz WiFi CSI data from the public GaitID dataset [34] for human identification. This dataset captures walking patterns from multiple subjects using commercial WiFi devices in a bistatic setup. In our experiment, three subjects walk along different trajectories while being monitored by a fixed receiver, producing diverse Doppler signatures. Fig. 15(a)–(c) present Doppler-time spectrograms generated using the 3D FFT tensor method. We can see that the mirrored components are visible, resulting in ambiguous and duplicated motion features. After applying our position-based refinement, as shown in Fig. 15(d)–(f), these artifacts are notably reduced. The refined spectrograms retain the dominant periodic limb motions while removing symmetry-induced distortions, demonstrating the robustness and cross-platform applicability of our method.

VIII. CONCLUSION

This work presents *PowerSense*, a calibration-free and real-time passive tracking system operating on CSI power in a bistatic setup. By relying on CSI power, the system effectively mitigates distortions introduced by clock asynchrony and hardware imperfections, avoiding the need for complex antenna calibration. A lightweight 3D FFT framework is developed to jointly extract delay, AoA, and Doppler features, followed by target detection, outlier suppression, and EKF-based trajectory tracking. We further propose a position-refined micro-Doppler extraction module that suppresses mirrored artifacts and reveals fine-grained motion dynamics with high clarity. Extensive experiments demonstrate the real-time capability of PowerSense and its strong performance in both trajectory tracking and micro-Doppler analysis across a variety of human motion patterns.

REFERENCES

- [1] A. Zhang, M. L. Rahman, X. Huang, Y. J. Guo, S. Chen, and R. W. Heath, "Perceptive mobile networks: Cellular networks with radio vision via joint communication and radar sensing," *IEEE Vehicular Technology Magazine*, vol. 16, no. 2, pp. 20–30, 2020.
- [2] F. Liu, Y. Cui, C. Masouros, J. Xu, T. X. Han, Y. C. Eldar, and S. Buzzi, "Integrated sensing and communications: Toward dual-functional wireless networks for 6g and beyond," *IEEE journal on selected areas in communications*, vol. 40, no. 6, pp. 1728–1767, 2022.
- [3] S. Lu, F. Liu, Y. Li, K. Zhang, H. Huang, J. Zou, X. Li, Y. Dong, F. Dong, J. Zhu *et al.*, "Integrated sensing and communications: Recent advances and ten open challenges," *IEEE Internet of Things Journal*, 2024.
- [4] K. Wu, Z. Wang, S.-L. Chen, J. A. Zhang, and Y. J. Guo, "Isac: From human to environmental sensing," *IEEE Journal of Selected Topics in Electromagnetics, Antennas and Propagation*, vol. 1, no. 1, pp. 84–98, 2025.
- [5] Y. Xu, K. Wu, J. A. Zhang, Z. Wang, B. A. Jayawickrama, and Y. J. Guo, "Smartphone-based experimental analysis of rainfall effects on lte signal indicators," *Sensors*, vol. 25, no. 2, 2025. [Online]. Available: <https://www.mdpi.com/1424-8220/25/2/375>
- [6] K. Wu, J. Pegoraro, F. Meneghello, J. A. Zhang, J. O. Lacruz, J. Widmer, F. Restuccia, M. Rossi, X. Huang, D. Zhang *et al.*, "Sensing in bi-static isac systems with clock asynchronism: A signal processing perspective," *arXiv preprint arXiv:2402.09048*, 2024.
- [7] K. Qian, C. Wu, Y. Zhang, G. Zhang, Z. Yang, and Y. Liu, "Widar2.0: Passive human tracking with a single wi-fi link," in *ACM MobiSys*, 2018, pp. 350–361.
- [8] Z. Wang, J. A. Zhang, M. Xu, and J. Guo, "Single-target real-time passive wifi tracking," *IEEE Transactions on Mobile Computing*, vol. 2, no. 6, pp. 3724–3742, 2023.
- [9] Z. Wang, J. A. Zhang, H. Zhang, M. Xu, and J. Guo, "Passive human tracking with wifi point clouds," *IEEE Internet of Things Journal*, vol. 12, no. 5, pp. 5528–5543, 2025.
- [10] Y. Hu, K. Wu, J. A. Zhang, W. Deng, and Y. J. Guo, "Performance bounds for csi-ratio based bi-static doppler sensing in isac systems," in *2024 IEEE International Conference on Communications Workshops (ICC Workshops)*. IEEE, 2024, pp. 1535–1540.
- [11] J. Pegoraro, J. O. Lacruz, T. Azzino, M. Mezzavilla, M. Rossi, J. Widmer, and S. Rangan, "Jump: Joint communication and sensing with unsynchronized transceivers made practical," *IEEE Transactions on Wireless Communications*, 2024.
- [12] F. Meneghello, D. Garlisi, N. Dal Fabbro, I. Tinnirello, and M. Rossi, "Sharp: Environment and person independent activity recognition with commodity iee 802.11 access points," *IEEE Transactions on Mobile Computing*, vol. 22, no. 10, pp. 6160–6175, 2022.
- [13] N. Tadayon, M. T. Rahman, S. Han, S. Valaee, and W. Yu, "Decimeter ranging with channel state information," *IEEE Transactions on Wireless Communications*, vol. 18, no. 7, pp. 3453–3468, 2019.
- [14] I. Ahmad, A. Ullah, and W. Choi, "Wifi-based human sensing with deep learning: Recent advances, challenges, and opportunities," *IEEE Open Journal of the Communications Society*, vol. 5, pp. 3595–3623, 2024.
- [15] W. Jiang, D. Ma, Z. Wei, Z. Feng, P. Zhang, and J. Peng, "Isac-net: Model-driven deep learning for integrated passive sensing and communication," *IEEE Transactions on Communications*, vol. 72, no. 8, pp. 4692–4707, 2024.
- [16] Z. Wang, J. A. Zhang, K. Wu, M. Xu, and Y. J. Guo, "Towards siso bistatic sensing for isac," 2025. [Online]. Available: <https://arxiv.org/abs/2508.12614>
- [17] K. Wu, J. A. Zhang, X. Huang, and Y. J. Guo, "A low-complexity csi-based wifi sensing scheme for los-dominant scenarios," in *ICC 2023 - IEEE International Conference on Communications*, 2023, pp. 2747–2752.
- [18] J. Braunkfelds, G. Jakovels, I. Murans, A. Litvinenko, U. Senkans, R. Rumba, A. Onzuls, G. Valters, E. Lidere, and E. Plone, "Experimental study on lte mobile network performance parameters for controlled drone flights," *Sensors*, vol. 24, no. 20, p. 6615, 2024.
- [19] Y. Feng, Y. Xie, D. Ganesan, and J. Xiong, "Lte-based pervasive sensing across indoor and outdoor," in *Proceedings of the 19th ACM Conference on Embedded Networked Sensor Systems*, 2021, pp. 138–151.
- [20] —, "Lte-based low-cost and low-power soil moisture sensing," in *Proceedings of the 20th ACM Conference on Embedded Networked Sensor Systems*, 2022, pp. 421–434.
- [21] X. Li, J. A. Zhang, K. Wu, Y. Cui, and X. Jing, "Csi-ratio-based doppler frequency estimation in integrated sensing and communications," *IEEE Sensors Journal*, vol. 22, no. 21, pp. 20 886–20 895, 2022.
- [22] Y. Xie, J. Xiong, M. Li, and K. Jamieson, "md-track: Leveraging multi-dimensionality for passive indoor wi-fi tracking," in *The 25th Annual International Conference on Mobile Computing and Networking*, 2019, pp. 1–16.
- [23] J. A. Zhang, K. Wu, X. Huang, Y. J. Guo, D. Zhang, and R. W. Heath, "Integration of radar sensing into communications with asynchronous transceivers," *IEEE Communications Magazine*, vol. 60, no. 11, pp. 106–112, 2022.
- [24] T. Pető and R. Sella, "Adaptive clutter cancellation techniques for passive," *Topics in Radar Signal Processing*, p. 139, 2018.
- [25] M. A. Richards *et al.*, *Fundamentals of radar signal processing*. Mcgraw-hill New York, 2005, vol. 1.
- [26] D. Tahmouh, "Review of micro-doppler signatures," *IET Radar, Sonar & Navigation*, vol. 9, no. 9, pp. 1140–1146, 2015.
- [27] J. Lien, N. Gillian, M. E. Karagozler, P. Amihoud, C. Schwesig, E. Olson, H. Raja, and I. Poupyrev, "Soli: Ubiquitous gesture sensing with millimeter wave radar," *ACM Transactions on Graphics (TOG)*, vol. 35, no. 4, pp. 1–19, 2016.
- [28] V. C. Chen, *The micro-Doppler effect in radar*. Artech house, 2019.
- [29] C. Tang, W. Li, S. Vishwakarma, F. Shi, S. Julier, and K. Chetty, "Mdpse: Human skeletal motion reconstruction using wifi micro-doppler signatures," *IEEE Transactions on Aerospace and Electronic Systems*, vol. 60, no. 1, pp. 157–167, 2023.
- [30] Y. Liu, J. Zhang, Y. Chen, W. Wang, S. Yang, X. Na, Y. Sun, and Y. He, "Real-time continuous activity recognition with a commercial mmwave radar," *IEEE Transactions on Mobile Computing*, vol. 24, no. 3, pp. 1684–1698, 2025.
- [31] F. Miao, Y. Huang, Z. Lu, T. Ohtsuki, G. Gui, and H. Sari, "Wi-fi sensing techniques for human activity recognition: Brief survey, potential challenges, and research directions," *ACM Computing Surveys*, vol. 57, no. 5, pp. 1–30, 2025.
- [32] W. Yang, Z. Li, and S. Chen, "Environment independent gait recognition based on wi-fi signals," *IEEE Transactions on Mobile Computing*, 2025.
- [33] K. Chen, J. A. Zhang, Z. Wang, and Y. J. Guo, "Development of an uplink sensing demonstrator for perceptive mobile networks," in *2023 22nd International Symposium on Communications and Information Technologies (ISCIT)*. IEEE, 2023, pp. 191–196.
- [34] Y. Zhang, Y. Zheng, G. Zhang, K. Qian, C. Qian, and Z. Yang, "Gaitid: Robust wi-fi based gait recognition," in *Wireless Algorithms, Systems, and Applications: 15th International Conference, WASA 2020, Qingdao, China, September 13–15, 2020, Proceedings, Part I 15*. Springer, 2020, pp. 730–742.



Dr. Zhongqin Wang is currently a Postdoctoral Research Fellow in the School of Electrical and Data Engineering at the University of Technology Sydney (UTS). From 2022 to 2023, he worked as a Lecturer at the School of Information Engineering, Capital Normal University, Beijing, China. Before that, he was a Postdoctoral Research Associate at UTS from 2021 to 2022, and a Research Engineer at UTS from 2020 to 2021. He received his Ph.D. degree from the University of Technology Sydney in January 2021, and his M.S. degree from Nanjing University of Posts and Telecommunications, Nanjing, China, in 2014. His research interests include radio sensing and integrated sensing and communications (ISAC).



J. Andrew Zhang (M'04-SM'11) received the B.Sc. degree from Xi'an JiaoTong University, China, in 1996, the M.Sc. degree from Nanjing University of Posts and Telecommunications, China, in 1999, and the Ph.D. degree from the Australian National University, Australia, in 2004.

Currently, Dr. Zhang is a Professor in the School of Electrical and Data Engineering, University of Technology Sydney, Australia. He was a researcher with Data61, CSIRO, Australia from 2010 to 2016, the Networked Systems, NICTA, Australia from 2004 to 2010, and ZTE Corp., Nanjing, China from 1999 to 2001. Dr. Zhang's research interests are in the area of signal processing for wireless communications and sensing, with a focus on integrated sensing and communications. He has published more than 300 papers in leading journals and conference proceedings, and has won 6 best paper awards for his work, including in IEEE ICC2013. He is a recipient of CSIRO Chair's Medal and the Australian Engineering Innovation Award in 2012 for exceptional research achievements in multi-gigabit wireless communications.



Kai Wu (Member, IEEE) received the B.E. degree from Xidian University, Xi'an, China, in 2012, and the Ph.D. degree from Xidian University in 2019 and from the University of Technology Sydney (UTS), Sydney, Australia, in 2020. From Nov 2017 to Nov 2018, he was a visiting scholar at DATA61, Commonwealth Scientific and Industrial Research Organisation (CSIRO).

He is currently a Lecturer with the School of Electrical and Data Engineering (SEDE) and the Global Big Data Technologies Centre (GBDTC) at UTS. He is the system architect of the TPG-UTS Networking Sensing Lab. His research interests include space/time/frequency signal processing and its applications in radar and communications and their joint designs. He published an authored book on joint communications and sensing (JCAS), aka integrated sensing and communications (ISAC), in December 2022.

His UTS Ph.D. degree was awarded "Chancellor's List 2020." His Xidian PhD thesis was awarded the "Best Ph.D. Thesis Award 2019" by the Chinese Institute of Electronics. He was awarded the Exemplary Reviewer for IEEE TRANSACTIONS ON COMMUNICATIONS, 2021. He is a Tutorial Speaker of WCNC'20, ICC'20, ISCIT'23, and RadarConf'23, presenting JCAS fundamentals and advancement. He was the TPC and special session (Co-)Chair/Member of numerous international conferences, e.g., ICC'20-23 and ISCIT'23. He is serving as the EiC Assistant for the IEEE ISAC-ETI Newsletter. He is an Associate Editor for IEEE Trans. on Mobile Computing, and has been a Guest Editor for the Special Issues in IEEE Journals.

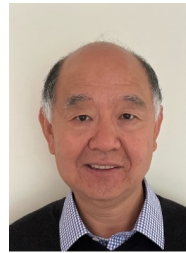


Kuangda Chen received the B.E. and M.E. degrees from Shanghai University, Shanghai, China, in 2005 and 2008, respectively, and the Master by research degree in electrical engineering from the University of Technology Sydney (UTS), Sydney, Australia, in 2024. Since 2024, he has been a Research Engineer with the RaSPA Laboratory. His research interests include design and implementation of laboratory communication systems for integrated sensing and communications (ISAC).



Min Xu (M'10) is currently a Professor at University of Technology Sydney. She received the B.E. degree from the University of Science and Technology of China, Hefei, China, in 2000, the M.S. degree from National University of Singapore, Singapore, in 2004, and the Ph.D. degree from University of Newcastle, Callaghan NSW, Australia, in 2010. Her research interests include multimedia data analytics, computer vision and machine learning. She has published over 100 research papers in high quality international journals and conferences. She has been

invited to be a member of the program committee for many international top conferences, including ACM Multimedia Conference and reviewers for various highly-rated international journals, such as IEEE Transactions on Multimedia, IEEE Transactions on Circuits and Systems for Video Technology and much more. She is an Associate Editor of Journal of Neurocomputing.



Y. Jay Guo (Fellow' 2014) received a Bachelor's Degree and a Master's Degree from Xidian University in 1982 and 1984, respectively, and a Ph.D Degree from Xian Jiaotong University in 1987, all in China. His current research interests include 6G antennas, mm-wave and THz communications and sensing systems as well as big data technologies such as deep machine learning and digital twin. He has published six books and over 800 research papers, and he holds 27 international patents.

Jay is a Fellow of the Australian Academy of Engineering and Technology, Royal Society of New South Wales and IEEE. He has won a number of the most prestigious Australian national awards. Together with his students and postdocs, he has won numerous best paper awards at international conferences such as IEEE AP-S, EuCAP and ISAP. He was a recipient of the prestigious 2023 IEEE APS Sergei A. Schelkunoff Transactions Paper Prize Award.

Jay is a Distinguished Professor and the founding Director of Global Big Data Technologies Centre (GBDTC) at the University of Technology Sydney (UTS), Australia. He is the founding Technical Director of the New South Wales (NSW) Connectivity Innovation Network (CIN). He is also the Founding Director of the TPG-UTS Network Sensing Lab. Before joining UTS in 2014, Prof Guo served as a Research Director in CSIRO for over nine years. Prior to CSIRO, he held various senior technology leadership positions in Fujitsu, Siemens and NEC in the U.K.